

# Sparse Unmixing-Based Change Detection for Multitemporal Hyperspectral Images

Alp Ertürk, *Member, IEEE*, Marian-Daniel Iordache, and Antonio Plaza, *Fellow, IEEE*

**Abstract**—In recent years, the increased availability of spectral libraries has resulted in a growing interest in sparse unmixing, which aims to find an optimal subset of library signatures to represent the pixels of remotely sensed hyperspectral datasets as linear combinations of these signatures. Sparse unmixing sidesteps two important drawbacks of the regular spectral unmixing process, namely the difficulty of estimating the number of endmembers, and the process of extracting the endmembers itself, the result of which will vary according to the utilized extraction method. In this work, sparse unmixing is exploited for the first time in the context of multitemporal hyperspectral data analysis and change detection. Change detection by sparse unmixing based on spectral libraries has the important advantage of providing not only pixel-level but also subpixel-level change information for the hyperspectral data. The changes that occur in multitemporal datasets due to time or as a result of a significant event are revealed, at subpixel-level, as the abundances of underlying endmembers within a pixel, or as variations in the distribution of these endmembers throughout the scene. The proposed approach is validated by experimental studies on both carefully prepared synthetic datasets and real datasets, using different spectral libraries.

**Index Terms**—Change detection, hyperspectral imaging, multitemporal data, sparse unmixing.

## I. INTRODUCTION

**H**YPERSPECTRAL images consist of pixels that are not the response of single underlying materials, but rather the combinations of a set of pure spectral signatures, termed *endmembers* in the literature. This is due to limited spatial resolution of imaging spectrometers or microscopic mixture effects [1]. *Spectral unmixing* is the process of decomposing each pixel of a hyperspectral image into a set of fractional abundances for these endmember signatures [2]. There is now a large number of approaches and methods for detecting the dimensionality of the data, i.e., the number of endmembers, extracting the endmembers, and calculating the abundance of endmembers for each pixel. A review of the different approaches and methods can be found in [1].

Manuscript received February 09, 2015; revised August 16, 2015; accepted August 31, 2015. Date of publication September 22, 2015; date of current version February 09, 2016. This work was supported by the Scientific and Technical Research Council of Turkey (TÜBİTAK).

A. Ertürk is with Kocaeli University Laboratory of Image and Signal Processing (KULIS), Kocaeli University, İzmit 41380, Turkey (e-mail: alp.erturk@kocaeli.edu.tr).

M.-D. Iordache is with the Flemish Institute for Technological Research (VITO), Center for Remote Sensing and Earth Observation Processes (TAP), 2400 Mol, Belgium (e-mail: marian-daniel.iordache@vito.be).

A. Plaza is with the Hyperspectral Computing Laboratory, Department of Technology of Computers and Communications, University of Extremadura, E-10003 Cáceres, Spain (e-mail: aplaza@unex.es).

Color versions of one or more of the figures in this paper are available online at <http://ieeexplore.ieee.org>.

Digital Object Identifier 10.1109/JSTARS.2015.2477431

However, in many cases, detecting the dimensionality of the data, and the identification of the real endmembers can be significantly challenging. This situation has led to semisupervised approaches in which the pixels are represented as combinations of spectral signatures from a library available *a priori* [3]. In this case, the problem amounts to detecting an optimal subset of a (potentially very large) spectral library, which can be used to accurately model each pixel in the scene [3]. For this purpose, an objective function which generally contains a sparsity-inducing regularizer is used to keep the number of regressors, i.e., the number of spectral signatures from the spectral library which contribute to the abundances, as small as possible. With the increase in the availability of spectral libraries, and the advantage of circumventing the challenges of regular spectral unmixing, sparse unmixing has gained much attention in recent years. Although sparse unmixing via variable splitting augmented Lagrangian (SUnSAL) [4] is the benchmark method used for this purpose, SUnSAL and other such methods mostly focus on spectral information and disregard the spatial information. Recent methods such as SUnSAL and total variation (SUnSAL-TV) [5] or nonlocal sparse unmixing (NLSU) [6] have been proposed to incorporate spatial information into sparse unmixing. SUnSAL-TV includes *a priori* spatial information in sparse unmixing by means of the TV regularizer [7], whereas NLSU exploits the spatial information among the possible predictions in the abundance maps. In the collaborative SUnSAL (CLSUnSAL) [8], sparsity is imposed for all pixels in the dataset simultaneously. In this work, sparse unmixing is utilized for the first time for change detection in multitemporal hyperspectral datasets.

Hyperspectral change detection is the process of detecting the changes that occur between the multiple hyperspectral data acquisitions from the same scene. These changes, whether due to seasonal or diurnal variations, or resulting from human activity or from a disaster or similar significant event, give rise to many applications such as environmental monitoring, urban planning, precision agriculture, or military surveillance [9]. Global linear predictors such as chronochrome (CC) [10], which is a linear prediction method that relies on using joint second-order statistics to calculate the linear transformation matrix between the two datasets, and covariance equalization (CE) [11], which is a similar method based on whitening that aims to reduce sensitivity to misregistration by not using the cross-covariance matrix, are benchmark change detection methods. An optional anomaly detection step can be used as postprocessing after applying these methods to detect only the anomalous changes. These approaches have been combined in a general framework in a hyperbolic anomaly change

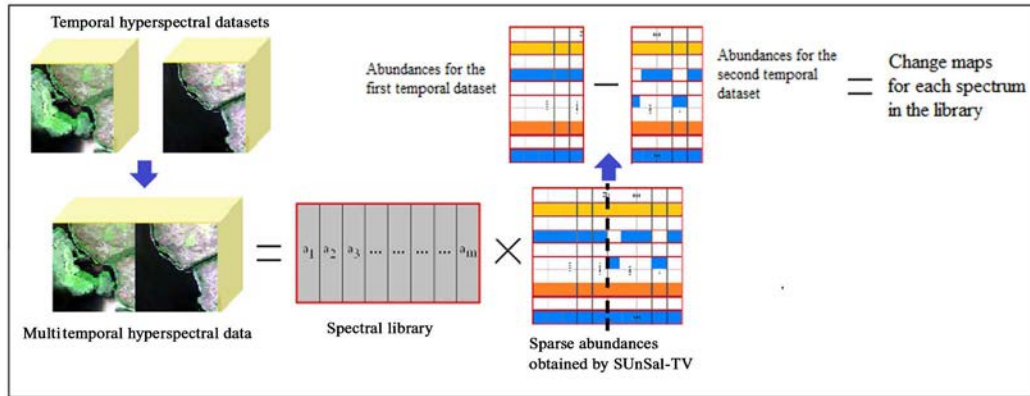


Fig. 1. Block diagram of the approach.

detector (HACD) [12], and improved in [13] to include elliptically contoured (EC) distributions, to address the fact that real data are generally not Gaussian. Other change detection methods include subspace-based change detection (SCD) [14], which detects pixel-wise changes by using the background subspace of the corresponding pixels in another image, and iteratively reweighted multivariate alteration detection (IR-MAD) [15], which relies on canonical variants to detect the changes. However, all these methods provide only the location of the change, but no information about the actual nature of the change. They also operate on a pixel-level basis, and do not account for subpixel-level information.

Hyperspectral change detection by spectral unmixing, in contrast, has the potential to provide easily interpretable information about the nature of the change, and also provide subpixel-level change information. The nature of the change can be a natural disaster such as a flood, which would amount to a significant increase in the abundance of “water” endmember throughout the scene, change in the cultivated crop in a farmland, which would result in the change of the prominent endmember in the region, settlement encroachment, i.e., increase in the abundance of man-made materials, or targets of interest, which would mean new and anomalous endmembers in the scene. However, even though hyperspectral change detection by unmixing has the important advantage of providing subpixel-level results and information on the nature of the change, it is still in an early stage in the literature, with most studies being limited to case studies. A general framework for change detection by spectral unmixing is proposed in [16]. Subpixel-level change detection by unmixing is utilized for a case study in [17]. Land-cover mapping by unmixing is discussed in [18]. Change detection by spectral unmixing is examined in detail and the subpixel-level information on the nature of the change that such an approach provides are presented by the authors in a recent work [19].

In this work, sparse unmixing is utilized for the first time for change detection in multitemporal hyperspectral datasets. Sparse unmixing, used in conjunction with spectral libraries, circumvents the drawbacks of regular spectral unmixing, while still providing subpixel-level detection and information on the nature of the change by obtaining a separate change map for each endmember. These features exhibit the potential to provide

additional valuable information with regard to existing change detection techniques.

This paper is organized as follows. Section II describes the proposed methodology for change detection in multitemporal hyperspectral datasets by sparse unmixing. Experimental results are provided in Sections III and IV for synthetic and real datasets, respectively. Conclusion and hints at plausible future studies are presented in Section V.

## II. METHODOLOGY

In this work, sparse unmixing is utilized for change detection in multitemporal hyperspectral images. For this purpose, temporal hyperspectral images are spatially merged into a single multitemporal hyperspectral data stack, and sparse unmixing with a spectral library is applied on the whole stack as shown in Fig. 1. Sparse unmixing is applied on the whole multitemporal data so that the resulting sparse solutions do not vary greatly between the temporal datasets.

SUnSAL-TV, which includes spatial information in the spectral-based processing of SUnSAL, is selected as the sparse unmixing method in this work. Assuming a linear mixing model, SUnSAL-TV solves the following optimization problem:

$$\min_{\mathbf{X}} \frac{1}{2} \|\mathbf{A}\mathbf{X} - \mathbf{Y}\|_F^2 + \lambda \|\mathbf{X}\|_{1,1} + \lambda_{TV} \text{TV}(\mathbf{X}) \quad (1)$$

$$\text{subject to } \mathbf{X} \geq 0$$

$$\text{TV}(\mathbf{X}) \equiv \sum_{\{i,j\} \in \varepsilon} \|\mathbf{X}_i - \mathbf{X}_j\| \quad (2)$$

where  $\text{TV}(\mathbf{X})$  is a vectorial extension of nonisotropic TV, which promotes piecewise smooth transitions in the fractional abundance of the same endmember among neighboring pixels.  $\varepsilon$  denotes the set of horizontal and vertical neighbors in the image,  $\mathbf{A}$  denotes a spectral library available *a priori*,  $\mathbf{X}$  is the matrix of fractional abundances, in which  $\mathbf{X}_i$  is the abundance vector of the pixel  $i$ , and  $\mathbf{Y}$  is the observed data.

In (1), the first term ensures a low reconstruction error, the second term imposes the sparsity constraint on the matrix of abundances, while the third term enforces spatial homogeneity of the abundance maps. The two regularization parameters  $\lambda$

and  $\lambda_{TV}$  weight the contribution of the last two terms in the optimization function. In this work, throughout all the tests, the  $\lambda$  and  $\lambda_{TV}$  parameters of SUnSAL-TV have been taken as 0.0001 and 0.03, respectively, for simplicity. The maximum number of iterations for SUnSAL-TV was empirically fixed to 200.

It should be noted that any spectral library can be used with our proposed sparse unmixing approach. However, the better the signatures in the library relate to the data (or to the characteristics of the sensor used to acquire the data), the better the performance of the method. To demonstrate this point, two different spectral libraries are utilized in this work. Another important aspect to note is that the signatures in the library generally require a preprocessing step in which the number of spectral bands of the signatures are downgraded (convolved) to the number of bands of the data. In this work, this downgrading is done with respect to the wavelength information of the spectral bands of the data, using a nearest neighbor approach. In other words, for each signature, the bands with the closest wavelengths with regard to those of the real data are selected. Then, a simple Gaussian filter is used to smooth the resulting signatures and remove any discontinuities.

After applying sparse unmixing, the resulting sparse solutions with endmembers and abundances are divided/assigned into their corresponding temporal datasets. In this step, any change between the temporal datasets is revealed, either as a library spectral signature that is obtained for one temporal dataset and not for the other, or as a change in the abundance of library spectra that exist in both temporal datasets. It is also possible to examine the abundance map obtained for each library spectra in each temporal dataset, the variation of which can be detected by a simple difference operation. The resulting variations in the abundance maps constitute the change map for that given library spectra. The overall change map is thus calculated by simple summation of the change maps for each library spectra.

### III. EXPERIMENTAL RESULTS ON SYNTHETIC DATA

#### A. Synthetic Dataset 1

The first synthetic multitemporal dataset used in our experiments has been simulated from the *Fractal 1* synthetic data.<sup>1</sup> *Fractal 1* image has 221 spectral bands and its size in pixels is  $100 \times 100$ . It contains nine endmember mineral signatures, which are originally from U.S. Geological Survey (USGS) spectral library.<sup>2</sup> These mineral signatures are presented in Fig. 2.

A synthetic temporal hyperspectral dataset is constructed in this work by modifying the abundances of the endmembers in a region, so that *sphene* mineral becomes more prominent, while *alunite*, *halloysite*, and *pyrophyllite* minerals decrease in abundance. This modification is both defined at pixel-level and subpixel-level, depending on the location. The original dataset

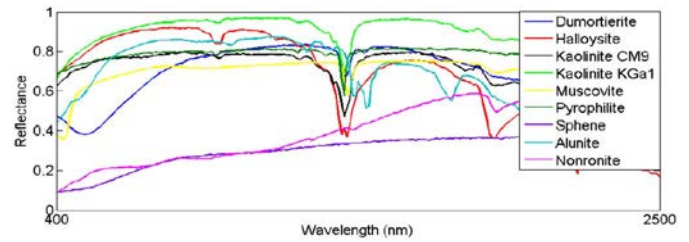


Fig. 2. Endmember signatures of *Fractal 1* data.

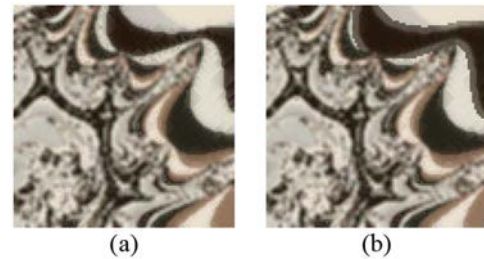


Fig. 3. Color images for the temporal datasets of *Fractal 1* for (a) first temporal dataset and (b) second temporal dataset.

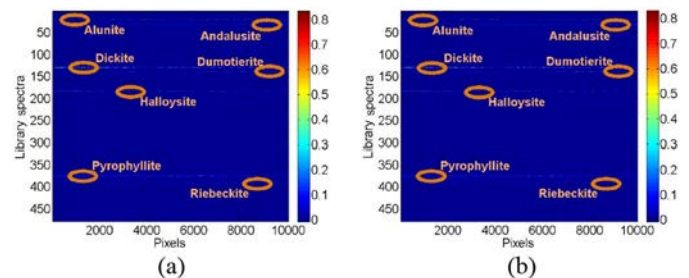


Fig. 4. Abundances for the temporal datasets of *Fractal 1* for (a) first temporal dataset and (b) second temporal dataset.

and the modified dataset are taken as the two temporal hyperspectral datasets. Color images of the temporal datasets are provided in Fig. 3.

Additive Gaussian white noise with 30-dB signal-to-noise ratio (SNR) is added to each temporal dataset before processing. The mineral signatures in the USGS spectral library are used with SUnSAL-TV for a library size of 478 spectra. The abundances obtained by the proposed approach for both temporal datasets are presented in Fig. 4. The small number of spectra that are prominent reveals the sparseness of the solution provided by the proposed approach. Whereas the subset of prominent spectra obtained by our approach does not perfectly match the endmembers in the data one-to-one, two of the endmembers that have varying abundances between the two temporal datasets, *alunite* and *pyrophyllite*, have been detected by our approach.

A performance comparison is conducted qualitatively by observing the final change maps, and quantitatively by receiver-operating-characteristic (ROC) curves, which are calculated based on a manually prepared ground truth map. The performance of the proposed change detection by sparse unmixing approach is compared with spectral angle distance (SAD), CC, HACD, and IR-MAD methods. It should be noted that

<sup>1</sup>[Online]. Available: <http://www.hypercomp.es/hypermix>

<sup>2</sup>[Online]. Available: <http://speclab.cr.usgs.gov/spectral-lib.html>

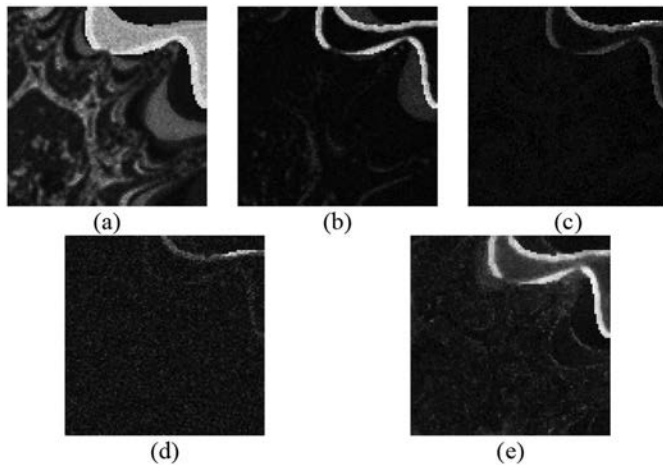


Fig. 5. Final change maps for the *Fractal 1* by (a) SAD; (b) CC; (c) HACD; (d) IR-MAD; and (e) sparse unmixing.

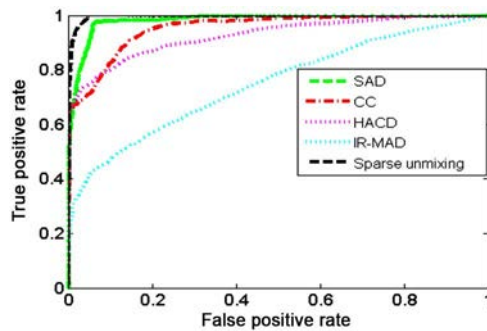


Fig. 6. ROC curves for *Fractal 1*.

IR-MAD is a method developed for multispectral images, and its performance for hyperspectral images would increase if a regularization is applied to the data prior to processing. Nevertheless, the author's codes have been used directly in this work, without any regularization step added to the codes.

The final change maps are presented in Fig. 5, and the ROC curves are given in Fig. 6. Note that the final change map for the proposed approach is obtained by simple summation of the change maps obtained for each endmember. It can be observed that the proposed method provides the best results overall.

### B. Synthetic Dataset 2

The second synthetic multitemporal dataset is simulated from the well-known ROSIS Pavia University data [20]. The spatial resolution of the dataset is 1.3 m, and the spectral resolution is 4 nm. The area around the metal building in the scene is extracted as the first temporal dataset. Its size is  $120 \times 70$  pixels, with 103 spectral bands. A second synthetic temporal dataset is simulated in a way that the vegetation regions between the parts of the building are manually modified to dirt, the information of which is extracted from the region around the building. This modification is done in terms of abundances, i.e., at subpixel-level, and also gradually so that diagonally the upper leftmost parts of the image have more variation in

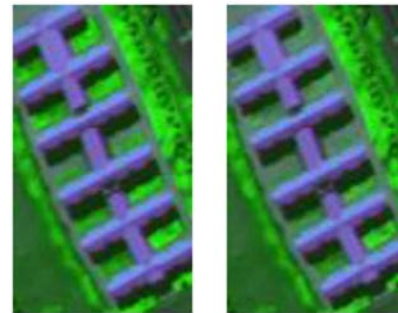


Fig. 7. RGB images for the first synthetic dataset.

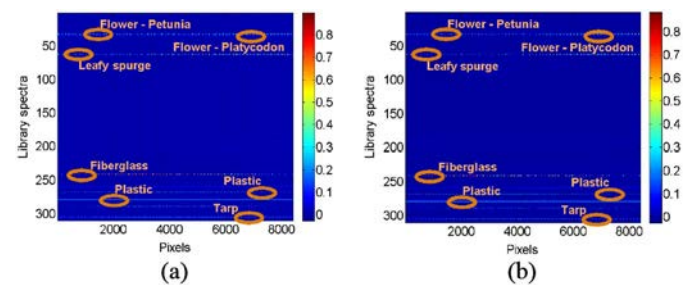


Fig. 8. Abundances for *Pavia Building* with USGS library for (a) first temporal dataset and (b) second temporal dataset.

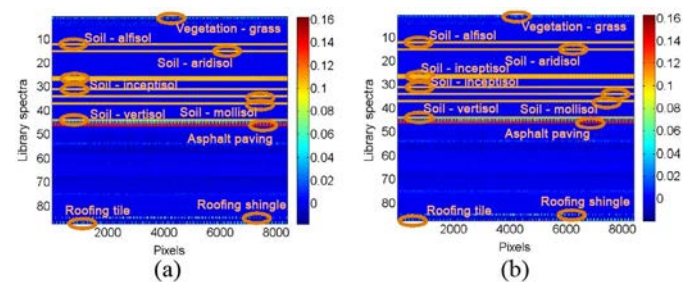


Fig. 9. Abundances for *Pavia Building* with ASTER library for (a) first temporal dataset and (b) second temporal dataset.

abundances than the lower rightmost parts. The multitemporal dataset is referred to hereinafter as *Pavia Building*. RGB images of the datasets are provided in Fig. 7.

Additive Gaussian white noise with 30-dB SNR is added to each temporal dataset before processing. The proposed change detection by sparse unmixing approach is evaluated for two different spectral libraries. The first spectral library is constructed from the USGS spectral library, with vegetation and man-made signatures, for a total spectra size of 310.

The second spectral library is constructed from the Advanced Spaceborne Thermal Emission and Reflection Radiometer (ASTER) spectral library,<sup>3</sup> using the vegetation, soils, and man-made spectral signatures for a total of 87 spectra. Note that only the spectra in the range of the wavelengths of the data are included. The abundances obtained by the proposed approach are presented in Figs. 8 and 9, for the two spectral

<sup>3</sup>[Online]. Available: <http://speclib.jpl.nasa.gov>

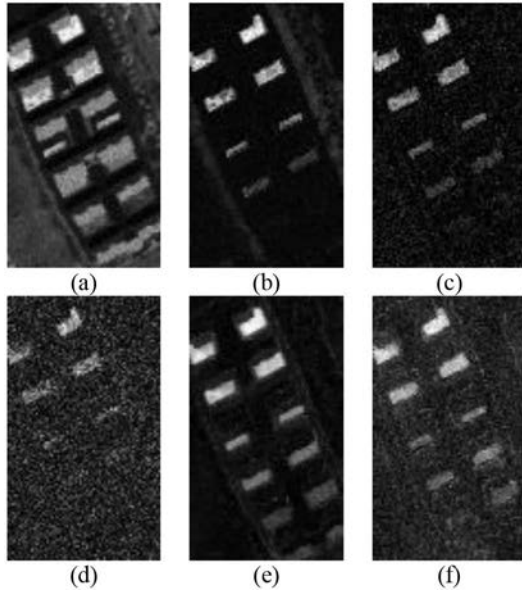


Fig. 10. Final change maps for *Pavia Building* by using: (a) SAD; (b) CC; (c) HACD; (d) IR-MAD; (e) sparse unmixing with USGS library; and (f) sparse unmixing with ASTER library.

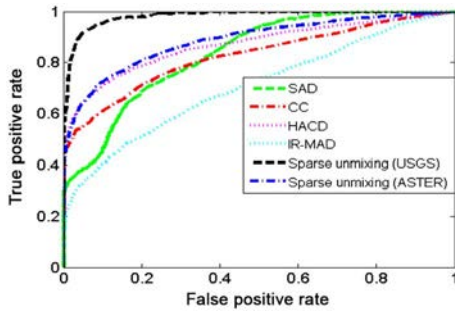


Fig. 11. ROC curves for *Pavia Building*.

libraries, respectively. Sparseness can again be observed in the obtained solutions.

It should be noted that the signatures in the library do not directly match the data. Hence, when USGS library is used, the prominent spectra are obtained to be *nylon* and *plastic* for the vegetation in the scene, and *fiberglass* for the building. When the ASTER library is used, the spectra match the data better, and the prominent spectra are found to be *vegetation-grass*, *vegetation-trees*, *asphalt*, and *roofing tile*, in addition to some abundances in different soil types.

The final change maps obtained by the proposed approach, and by the other methods used for performance comparisons, are presented in Fig. 10. A high amount of false alarms can be observed for SAD. CC gives a cleaner result, but misses the subtle, i.e., subpixel-level, changes. HACD performs somewhat better than CC, as expected. IR-MAD provides very noisy results, whereas the proposed approach performs the best overall with the spectral library of USGS. This can also be observed from the ROC curves, based on a manually prepared ground truth map, provided in Fig. 11.

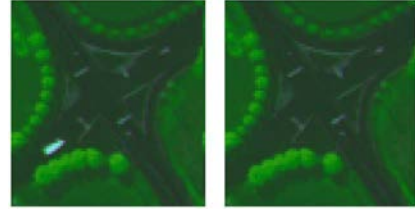


Fig. 12. RGB images for *Pavia Car*.

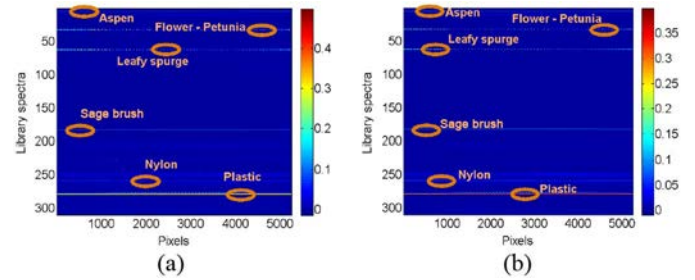


Fig. 13. Abundances for *Pavia Car* with USGS library for (a) first temporal dataset and (b) second temporal dataset.

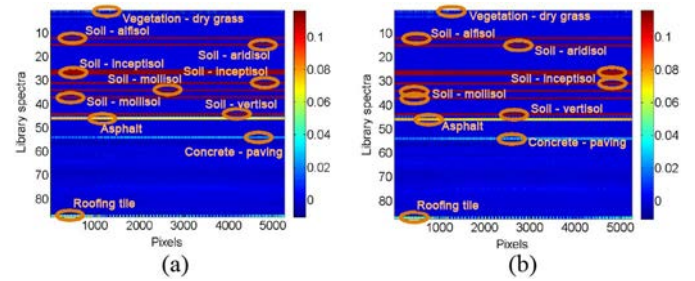


Fig. 14. Abundances for *Pavia Car* with ASTER library for (a) first temporal dataset and (b) second temporal dataset.

### C. Synthetic Dataset 3

The third synthetic multitemporal dataset is also formed from the ROSIS Pavia University data. The area around a crossroads in the scene is taken as the first temporal dataset. The dataset comprises  $75 \times 70$  pixels in size, with 103 spectral bands. In the second synthetic temporal dataset, the vehicle in the scene is carefully removed and the pixels in the corresponding locations are modified to pixels belonging to the road in the background. In addition, the pixels that are directly around the vehicle are also modified at subpixel-level, to remove the shadow effects. The multitemporal dataset is referred hereinafter as *Pavia Car*. RGB images are provided in Fig. 12. Additive Gaussian white noise is added to each dataset in 30-dB SNR before processing. The abundance maps for each temporal dataset are provided in Figs. 13 and 14, for the two spectral libraries used, which are the same as in the previous synthetic data experiment.

In this case, when the spectral library is constructed from the USGS signatures, the prominent spectra in the datasets are found to be *aspen*, *flower-petunia*, *leafy spurge*, *sagebrush*, *plastic*, and *nylon*. The change is observed to be mostly located on spectra that are identified as *cyanide*, *fiberglass*, *insulation*, and *tarp*.

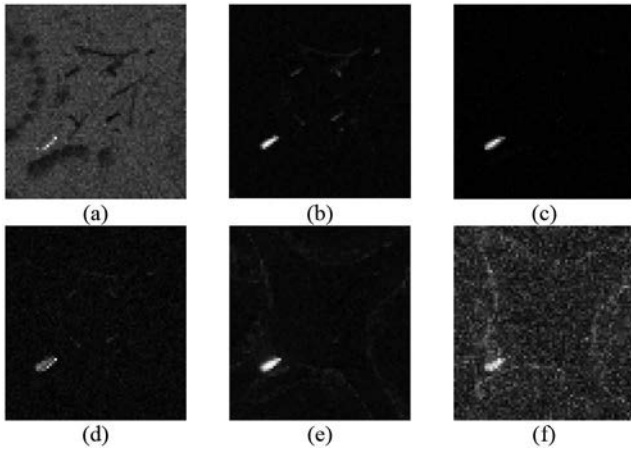


Fig. 15. Final change maps for *Pavia Car* by using: (a) SAD; (b) CC; (c) HACD; (d) IR-MAD; (e) sparse unmixing with USGS library; and (f) sparse unmixing with ASTER library.

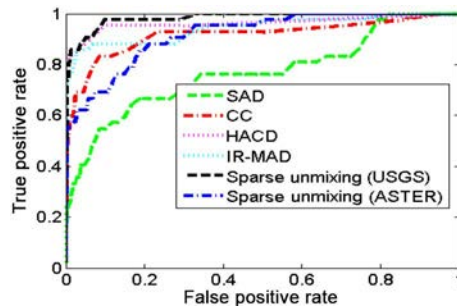


Fig. 16. ROC curves for *Pavia Car*.

When the spectral library is constructed from ASTER signatures, the prominent spectra are observed to be located in spectra such as different kinds of soil, *asphalt*, *concrete* and *roofing tile*, and some abundance also for *vegetation-grass* and *vegetation-trees* signatures with significant changes occurring for the *concrete* and *construction marble* spectra.

The final change maps are provided in Fig. 15. It can be observed that SAD performs the worst in this particular case. For the proposed method, it can be observed that the performance is much better with the spectral library formed from the USGS library, as compared to the ASTER library. The performance exhibited by the other methods appears to be comparable.

In Fig. 16, ROC curves are provided, based on a manually prepared ground truth. It can be seen that HACD and IR-MAD have performed well in this case, as the variations between the datasets are mostly at pixel-level instead of subpixel-level, but sparse unmixing with the USGS spectral library has performed better.

#### D. Synthetic Dataset 4

The fourth synthetic multitemporal dataset is simulated from the AVIRIS Salinas dataset. The temporal datasets are of size  $217 \times 217$  pixels, with 204 spectral bands. The spatial resolution of the datasets is 3.7 m. A subset of the AVIRIS Salinas



Fig. 17. RGB images for the *Salinas* dataset.

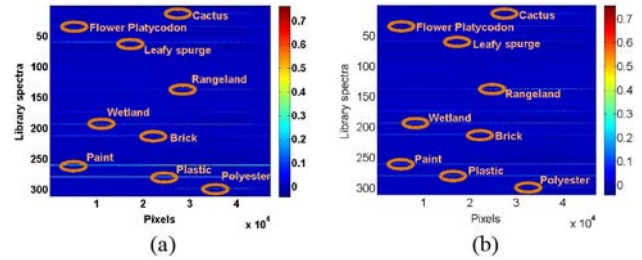


Fig. 18. Abundances for *Salinas* with USGS library for (a) first temporal dataset and (b) second temporal dataset.

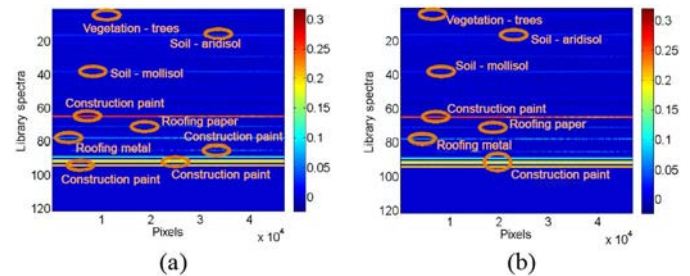


Fig. 19. Abundances for *Salinas* with ASTER library for (a) first temporal dataset and (b) second temporal dataset.

data is selected as the first temporal dataset. For the second temporal dataset, the pixels in the region at the bottom of the scene (belonging to *Broccoli green weeds* class) are modified into pixels in the *Celery* class region, randomly. Note that this variation is purely at pixel-level, i.e., there is no subpixel-level variation between the temporal datasets. Ground truth data information for the AVIRIS Salinas data is available in [20]. RGB images are provided in Fig. 17.

Additive Gaussian white noise is later added to each temporal dataset with 30-dB SNR. Two spectral libraries are constructed, one from the vegetation and man-made signatures of the USGS spectral library, for a total library size of 310, and the other from the vegetation, soil, and man-made signatures of the ASTER library for a total number of 121 spectra. The abundance maps for each temporal dataset are provided in Figs. 18 and 19. The prominent spectra in the datasets are observed to be *flower-platycodon*, *lawn grass*, *leafy spurge*, *rangeland*, *wetland*, *brick*, *paint*, *plastic*, and *polyester* from the library from USGS, and *vegetation-trees*, *soil-mollisol*, *soil-aridisol*, *construction paint*, *roofing-metal*, *roofing-paper*, and *roofing-shingle* from the library from ASTER. Note that the ASTER spectral library contains only four vegetation signatures in total, which prevents the representation of the data in a similar way to the ground truth.

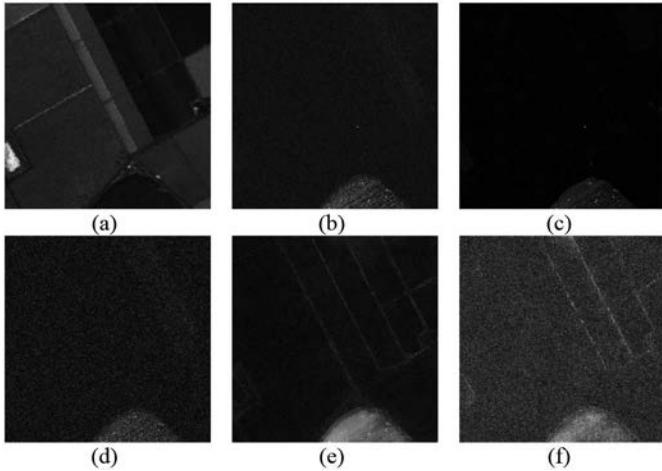


Fig. 20. Final change maps for *Salinas* by (a) SAD; (b) CC; (c) HACD; (d) IR-MAD; (e) sparse unmixing with USGS library; and (f) sparse unmixing with ASTER library.

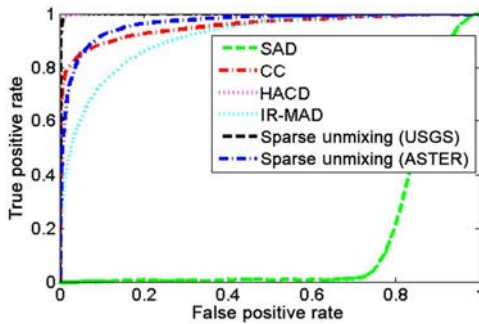


Fig. 21. ROC curves for the *Salinas*.

Fig. 20 gives a comparison between the final change maps. It can be observed that the simple SAD metric performs very poorly in this dataset. HACD seems to provide the cleanest result in terms of false alarms, followed closely by sparse unmixing with the spectral library based on USGS spectral library. ROC curves based on the ground truth map are provided in Fig. 21. HACD performs the best in this experiment, followed very closely by sparse unmixing with the USGS library. CC and sparse unmixing with the ASTER library perform comparably and better than IR-MAD.

#### IV. EXPERIMENTAL RESULTS ON REAL DATA

##### A. Real Dataset 1

For the first experimental study on real data, subsets of two AVIRIS datasets that are available in the AVIRIS database [21] are used. The datasets are from the New Orleans area, acquired in the dates of September 2010 and October 2011. The spatial resolution of the datasets is around 3.4 m. RGB images of the temporal datasets are provided in Fig. 22.

The first spectral library is constructed from the vegetation and volatiles signatures from the USGS spectral library for a total number of 224 spectra. The second spectral library is constructed from the water/snow/ice, vegetation, and soil signatures from the ASTER library for a total number of 52 spectra.

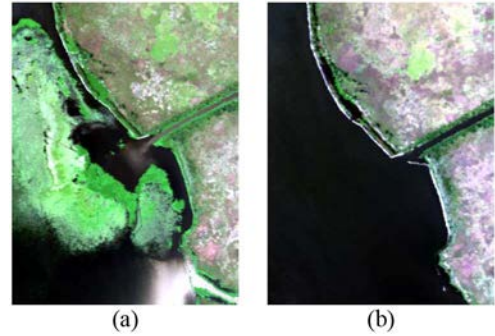


Fig. 22. RGB images for *New Orleans*: (a) September 2010 and (b) October 2011.

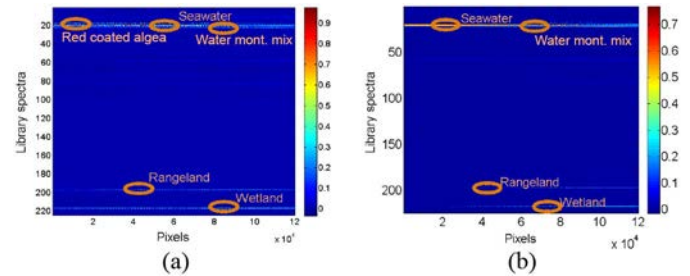


Fig. 23. Abundances for *New Orleans* with USGS library for (a) first temporal dataset and (b) second temporal dataset.

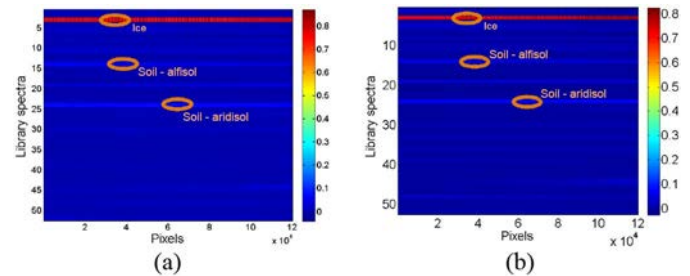


Fig. 24. Abundances for *New Orleans* with ASTER library for (a) first temporal dataset and (b) second temporal dataset.

The abundances obtained by the sparse unmixing approach for both temporal datasets and spectral libraries are provided in Figs. 23 and 24. Using the library from USGS, the most prominent spectra in the datasets are found to be *red coated algae water*, *open ocean seawater*, *water and montmor mixture*, *leafy spurge*, *rangeland*, and *wetland* signatures. The variation between the datasets in this case is very clear in terms of spectra, and the abundance of watery signatures increases, while the abundance of *rangeland*, *wetland*, and *leafy spurge* decreases in the locations that exhibit the change. This result is mostly compatible with the change in the given multitemporal dataset.

Using the library from ASTER, the most significant spectra are obtained to be *ice*, with the most significant variation in abundance between the two temporal datasets obtained for *ice*, *vegetation-trees*, and *soil-aridisol*. This matching to the *ice* signature is probably caused by a discrepancy between the spectral signatures in the ASTER database, and this dataset. In other words, the ASTER spectral library is inadequate in representing this dataset in a good way. As can be observed from

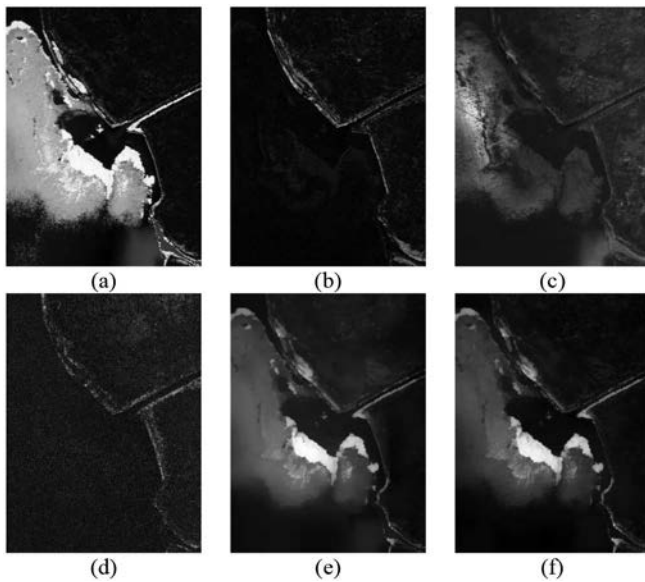


Fig. 25. Final change maps for *New Orleans* by (a) SAD; (b) CC; (c) HACD; (d) IR-MAD; (e) sparse unmixing with USGS library; and (f) sparse unmixing with ASTER library.

the case when the USGS spectral library is utilized, a spectral library that can better match the spectra in the data overcomes this possible shortcoming, which would also not occur with a mission-specific spectral library.

The final change maps, along with the change maps obtained with the other utilized methods, are provided in Fig. 25. It can be seen that CC and IR-MAD have provided the worst results for these datasets. The change maps obtained by SAD, HACD, and the final change maps obtained by the proposed change detection by sparse unmixing appear comparable.

In order to be able to provide a quantitative assessment of performance, ground truth maps have been prepared in this work for this dataset, by a combination of automatic data clustering and manual work. Two possible ground truth maps, and the ROC curves resulting from the utilization of each, are provided in Figs. 26 and 27. One of the ground truth maps can be considered as “easy” or pixel-level, while the second ground truth map can be considered as “challenging” or containing subpixel-level changes. While these ground truth maps are not perfect, they enable a relatively reliable and fair quantitative assessment of performance. It can be observed from the ROC curves that the simple SAD method outperforms all the other methods, whereas the performance of the proposed approach comes a close second. Note that neither of the other methods provide information on the nature of the change, as the proposed approach does.

### B. Real Dataset 2

For the second experimental study using real data, APEX data acquired over Kalmthout, Belgium, are utilized. The area of interest contains a forest fire that occurred in May 23, 2011. Because the flight lines are different before and after the fire occurs, two different hyperspectral datasets, acquired in June 2010, have been merged, i.e., mosaicked in this work to obtain

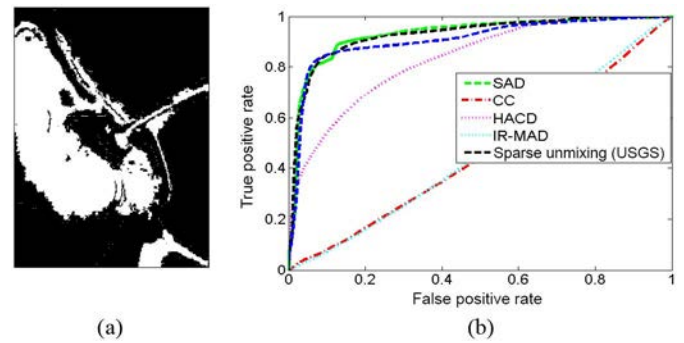


Fig. 26. Quantitative performance assessment for *New Orleans*. (a) Ground truth map. (b) ROC curves.

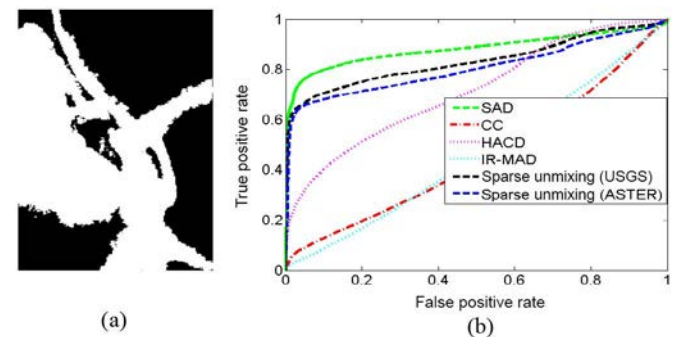


Fig. 27. Second quantitative performance assessment for *New Orleans*. (a) Ground truth map. (b) ROC curves.

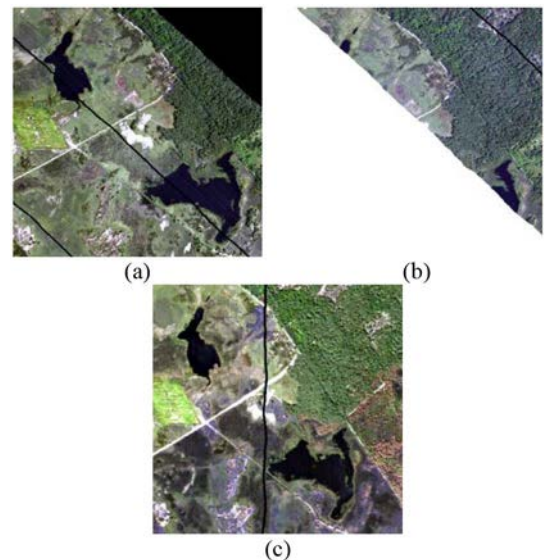


Fig. 28. RGB images for *Kalmthout*. (a) June 2010, first flight line data. (b) June 2010, second flight line data. (c) June 2011.

the first temporal dataset. The second temporal dataset belongs to a single flight line of hyperspectral data, acquired in June 2011. The datasets have 295 spectral bands, but in this work the bands with low SNR are eliminated, resulting in 245 spectral bands. RGB images of the two temporal datasets are presented in Fig. 28.

Two spectral libraries, one constructed from the vegetation and volatiles signatures from the USGS spectral library

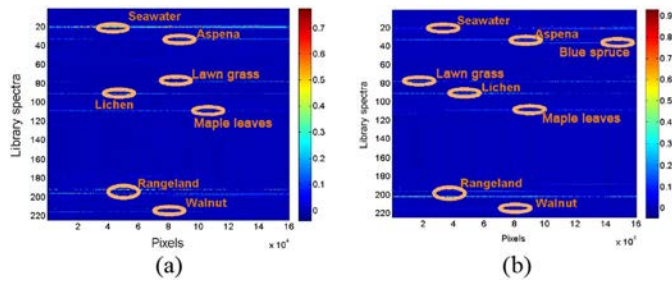


Fig. 29. Abundances for *Kalmthout* with USGS library for (a) first temporal dataset and (b) second temporal dataset.

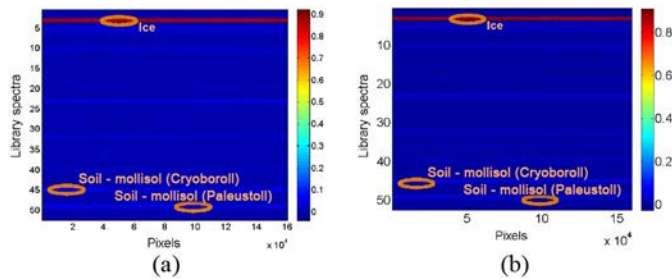


Fig. 30. Abundances for *Kalmthout* with ASTER library for (a) first temporal dataset and (b) second temporal dataset.

for a total number of 224 spectra, and the other from the water/snow/ice, vegetation, and soil signatures from the ASTER library for a total number of 52 spectra, are used with the proposed approach. The abundances obtained for both temporal datasets are shown in Figs. 29 and 30. For the spectral library based on the USGS library, the main variations between the datasets were found to be in the water and rangeland signatures. For the ASTER spectral library, again the spectral signature of *ice* appears prominent in both temporal datasets and for the variation.

The final change maps obtained by SAD, CC, HACD, IR-MAD, and the proposed method are presented in Fig. 31. The interferers resulting from the flight lines were removed from the change maps by postprocessing, as they were detected as changes also. A reference map, extracted from a news article about the fire, is presented in Fig. 32. By qualitatively comparing the change maps with the reference map, it can be stated that SAD presents the best results overall in this particular case. A drawback of the proposed approach for this dataset is that neither of the utilized spectral libraries contain spectral signatures for burned area/vegetation, which limit the performance of the proposed approach in this particular case. It should be anticipated that the performance of the proposed method would increase with a spectral library that includes signatures of forest fire or burned vegetation.

In order to be able to provide a quantitative assessment of performance, ground truth maps have been prepared in this work for this dataset, by using the reference map in Fig. 32 and manual work, following in-depth discussions with researchers who have been to the area immediately after the fire. Two possible ground truth maps, and the ROC curves resulting from the utilization of each, are provided in Figs. 33 and 34.

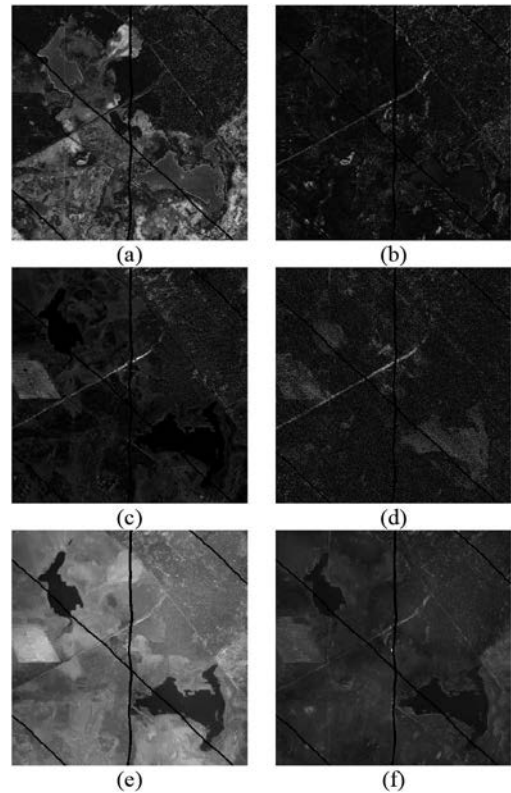


Fig. 31. Final change maps for *Kalmthout* by (a) SAD; (b) CC; (c) HACD; (d) IR-MAD; (e) sparse unmixing with USGS library; and (f) sparse unmixing with ASTER library.



Fig. 32. Reference map for *Kalmthout*.

One of the ground truth maps can be considered as “easy” or pixel-level, while the second ground truth map can be considered as “challenging” or containing subpixel-level changes. While these ground truth maps are not perfect, nevertheless they enable a relatively reliable and fair quantitative assessment of performance. It can be observed from the ROC curves that the data are more challenging and the performances of the methods are lower.

### C. Real Dataset 3

For the third experimental study using real data, spatial subsets of two EO-1 Hyperion datasets have been used. The datasets have been acquired over Athens, Greece, in September 2003 and September 2004. The spatial resolution of the datasets is 30 m, and the spatial size of the images is  $160 \times 160$  pixels. RGB images of the temporal dataset are provided in Fig. 35.

Two spectral libraries, one constructed from the vegetation, volatiles and man-made signatures from the USGS spectral

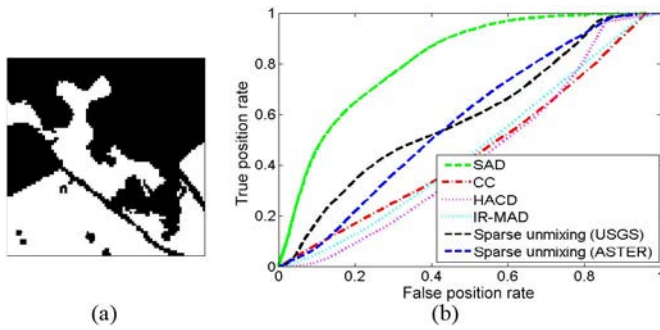


Fig. 33. Quantitative performance assessment for *Kalmthout*. (a) Ground truth map. (b) ROC curves.

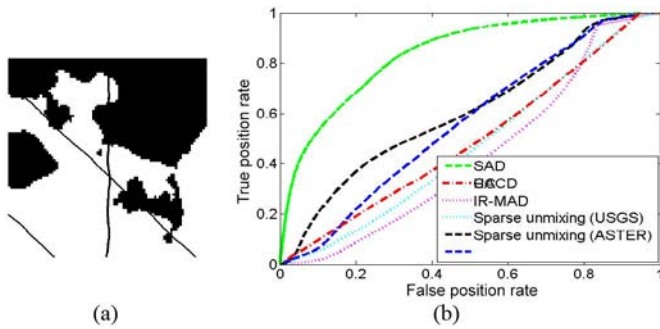


Fig. 34. Second quantitative performance assessment for *Kalmthout*. (a) Ground truth map. (b) ROC curves.

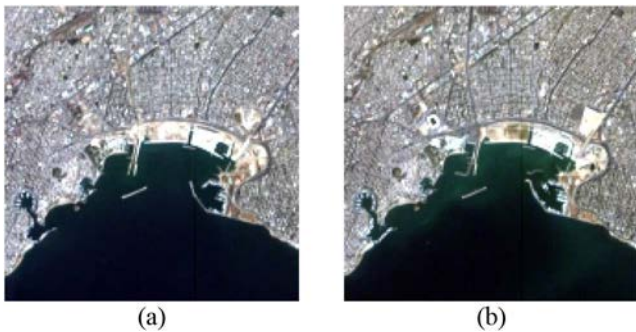


Fig. 35. RGB images for *Athens*: (a) September 2003 and (b) September 2004.

library (for a total number of 334 spectra), and the other from the water/snow/ice, vegetation, soil, and man-made signatures from the ASTER library (for a total number of 129 spectra), are used with the proposed approach. The abundances obtained for both temporal datasets are shown in Figs. 36 and 37. For the spectral library based on the USGS library, the main abundance variations between the datasets were found for various water signatures, metal sheet, vinyl plastic, petunia flower, and Reynolds tunnel sludge. For the ASTER spectral library, the main abundance variations in the scene are obtained for water, aridisol soil, and mollisol soil signatures.

The final change maps obtained by SAD, CC, HACD, IR-MAD, and the proposed method are presented in Fig. 38. It can be seen that SAD provides the best visual results overall. For quantitative assessment, a ground truth change map has

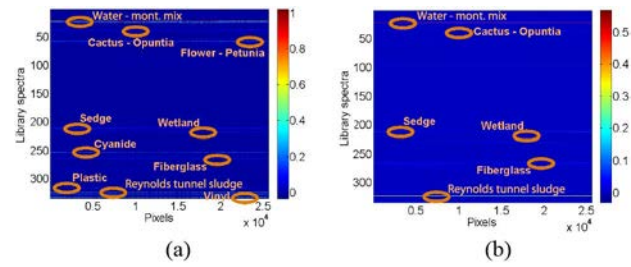


Fig. 36. Abundances for *Athens* with USGS library for (a) first temporal dataset and (b) second temporal dataset.

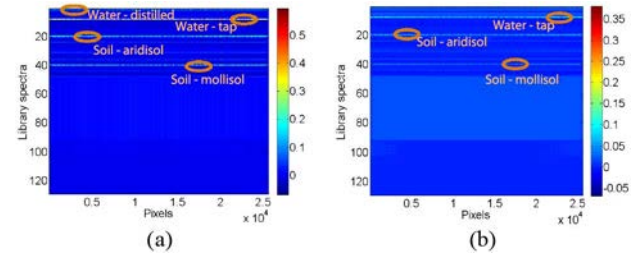


Fig. 37. Abundances for *Athens* with ASTER library for (a) first temporal dataset and (b) second temporal dataset.

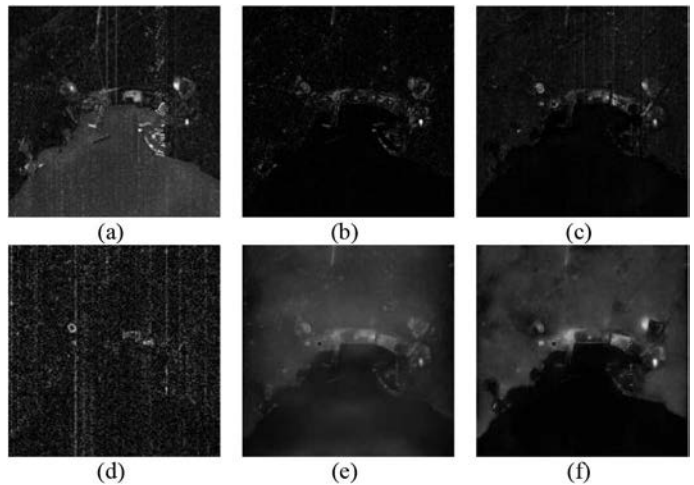


Fig. 38. Final change maps for *Athens* by (a) SAD; (b) CC; (c) HACD; (d) IR-MAD; (e) sparse unmixing with USGS library; and (f) sparse unmixing with ASTER library.

been prepared manually for the datasets. This ground truth map and the ROC curves obtained for each method are presented in Fig. 39. Note that, as again for the previous real dataset experiments, it is not claimed that the presented ground truth map is perfect. This process is merely conducted to provide quantitative performance assessment, in addition to providing visual results.

Provided in Table I are the area-under-curve (AUC) values for each ROC curve obtained in each experiment for each method. These values provide an overall quantitative evaluation for the proposed method and the methods used for comparison purposes.

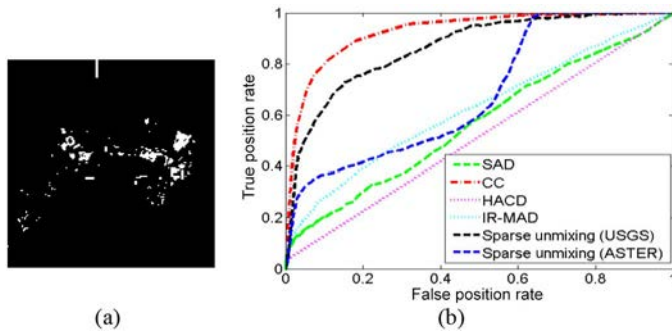


Fig. 39. Quantitative performance assessment for *Athens*. (a) Ground truth map. (b) ROC curves.

TABLE I  
AUC VALUES FOR EACH METHOD AND DATASET

	SAD	CC	HACD	IR-MAD	Sparse USGS	Sparse ASTER
Fractal	0.9831	0.9550	0.9264	0.7496	<b>0.9915</b>	—
Pavia Building	0.8364	0.8307	0.8751	0.6858	<b>0.9830</b>	0.8881
Pavia Car	0.7691	0.9161	0.9623	0.9434	<b>0.9874</b>	0.9188
Salinas	0.1583	0.9562	0.9992	0.9186	0.9996	<b>0.9668</b>
AVIRIS New Orleans—first GT	0.9311	0.4597	0.8353	0.4712	<b>0.9420</b>	0.9261
AVIRIS New Orleans—second GT	<b>0.8813</b>	0.4561	0.7166	0.4654	0.8665	0.8533
APEX Kalmthout—first GT	<b>0.8173</b>	0.4626	0.5406	0.4633	0.5939	0.5781
APEX Kalmthout—second GT	<b>0.8397</b>	0.4948	0.5525	0.4718	0.6085	0.5647
Hyperion Athens	0.5693	<b>0.9290</b>	0.5163	0.6249	0.8658	0.6896

## V. CONCLUSION AND FUTURE RESEARCH LINES

Sparse unmixing, supported by the increase of the number and availability of spectral libraries, has gained much attention in recent years, mainly because it circumvents the drawbacks of classic spectral unmixing. However, sparse unmixing has not been utilized for hyperspectral change detection purposes, which are important for many applications ranging from environmental monitoring to military surveillance. In this work, sparse unmixing is first explored in the context of change detection, using a large number of different synthetic and real datasets, and with multiple spectral libraries. The benefits of using sparse unmixing with spectral libraries for change detection are revealed, particularly when the library is related to the data. The proposed approach provides not only the prominent spectra in the datasets, hence giving information about the dataset itself, but also about the change in the abundances of the spectra, which provides extra information on the nature of change, instead of only providing the locations of change as in other methods. The proposed approach also provides increased change detection performance, especially

when the datasets contain subpixel-level changes. Future studies may include the incorporation of preprocessing approaches such as dictionary pruning or methods based on using *a priori* information about the data, as well as a more detailed investigation regarding the variability of endmember signatures with time.

## ACKNOWLEDGMENT

The authors would like to thank the Associate Editor and the Anonymous Reviewers for their outstanding comments and suggestions, which greatly helped us to improve the technical quality and presentation of this paper. They would also like to thank Dr. A. A. Nielsen for providing the MATLAB codes for IR-MAD, and Dr. J. Bioucas-Dias for providing the MATLAB codes for SUnSAL-TV.

## REFERENCES

- [1] J. M. Bioucas-Dias *et al.*, "Hyperspectral unmixing overview: Geometrical, statistical, and sparse regression-based approaches," *IEEE J. Sel. Topics Appl. Earth Observ. Remote Sens.*, vol. 5, no. 2, pp. 354–379, Apr. 2012.
- [2] N. Keshava and J. F. Mustard, "Spectral unmixing," *IEEE Signal Process. Mag.*, vol. 19, no. 1, pp. 44–57, Jan. 2002.
- [3] M.-D. Iordache, J. M. Bioucas-Dias, and A. Plaza, "Sparse unmixing of hyperspectral data," *IEEE Trans. Geosci. Remote Sens.*, vol. 49, no. 6, pp. 2014–2039, Jun. 2011.
- [4] J. M. Bioucas-Dias and M. Figueiredo, "Alternating direction algorithms for constrained sparse regression: Application to hyperspectral unmixing," in *Proc. 2nd Workshop Hyperspectral Image Signal Process. (WHISPERS)*, 2010, pp. 1–4.
- [5] M.-D. Iordache, J. M. Bioucas-Dias, and A. Plaza, "Total variation spatial regularization for sparse hyperspectral unmixing," *IEEE Trans. Geosci. Remote Sens.*, vol. 50, no. 11, pp. 4484–4502, Nov. 2012.
- [6] Y. Zhong, R. Feng, and L. Zhang, "Non-local sparse unmixing for hyperspectral remote sensing imagery," *IEEE J. Sel. Topics Appl. Earth Observ. Remote Sens.*, vol. 7, no. 6, pp. 1889–1909, Jun. 2014.
- [7] A. Chambolle, "An algorithm for total variation minimization and applications," *J. Math. Imag. Vis.*, vol. 20, nos. 1–2, pp. 89–97, Jan./Mar. 2004.
- [8] M.-D. Iordache, J. M. Bioucas-Dias, and A. Plaza, "Collaborative sparse regression for hyperspectral unmixing," *IEEE Trans. Geosci. Remote Sens.*, vol. 52, no. 1, pp. 341–354, Jan. 2014.
- [9] J. Meola, M. T. Eismann, R. L. Moses, and J. N. Ash, "Detecting changes in hyperspectral imagery using a model-based approach," *IEEE Trans. Geosci. Remote Sens.*, vol. 49, no. 7, pp. 2647–2661, Jul. 2011.
- [10] A. Schaum and A. Stocker, "Long-interval chronochrome target detection," in *Proc. Int. Symp. Spectral Sens. Res.*, 1998.
- [11] A. Schaum and A. Stocker, "Hyperspectral change detection and supervised matched filtering based on covariance equalization," *Proc. SPIE*, vol. 5425, pp. 77–90, 2004.
- [12] J. Theiler and S. Perkins, "Proposed framework for anomalous change detection," in *Proc. ICML Workshop Mach. Learn. Algorithms Surveill. Event Detect.*, Jun. 2006, pp. 7–14.
- [13] J. Theiler, C. Scovel, B. Wohlberg, and B. R. Roy, "Elliptically contoured distributions for anomalous change detection in hyperspectral imagery," *IEEE Geosci. Remote Sens. Lett.*, vol. 7, no. 2, pp. 271–275, Apr. 2010.
- [14] C. Wu, B. Du, and L. Zhang, "A subspace-based change detection method for hyperspectral images," *IEEE J. Sel. Topics Appl. Earth Observ. Remote Sens.*, vol. 6, no. 2, pp. 815–830, Apr. 2013.
- [15] A. A. Nielsen, "The regularized iteratively reweighted MAD method for change detection in multi- and hyperspectral data," *IEEE Trans. Image Process.*, vol. 16, no. 2, pp. 463–478, Feb. 2007.
- [16] Q. Du, L. Wassom, and R. King, "Unsupervised linear unmixing for change detection in multitemporal airborne hyperspectral imagery," in *Proc. Int. Workshop Anal. Multi Temporal Remote Sens. Images*, 2005, pp. 136–140.
- [17] C.-C. Hsieh, P.-F. Hsieh, and C.-W. Lin, "Subpixel change detection based on abundance and slope features," in *Proc. IEEE Int. Geosci. Remote Sens. Symp. (IGARSS)*, 2006, pp. 775–778.

- [18] R. Zurita-Milla, L. Gomez-Chova, L. Guanter, J. G. P. W. Clevers, and G. Camps-Valls, "Multitemporal unmixing of medium-spatial-resolution satellite images: A case study using MERIS images for land-cover mapping," *IEEE Trans. Geosci. Remote Sens.*, vol. 49, no. 11, pp. 4308–4317, Nov. 2011.
- [19] A. Ertürk and A. Plaza, "Informative change detection by unmixing for hyperspectral images," *IEEE Geosci. Remote Sens. Lett.*, vol. 12, no. 6, pp. 1252–1256, Jun. 2015.
- [20] Computational Intelligence Group. *Hyperspectral Remote Sensing Scenes*, Basque Univ., Leioa, Spain [Online]. Available: [http://www.ehu.es/ccwintco/index.php?title=Hyperspectral\\_Remote\\_Sensing\\_Scenes&re\\_direct=no](http://www.ehu.es/ccwintco/index.php?title=Hyperspectral_Remote_Sensing_Scenes&re_direct=no)
- [21] Jet Propulsion Laboratory, NASA. *2006–2014 AVIRIS Flight Locator Tool* [Online]. Available: [http://aviris.jpl.nasa.gov/alt\\_locator](http://aviris.jpl.nasa.gov/alt_locator)



**Alp Ertürk** (S'11–M'14) received the B.Sc. and M.Sc. degrees in electrical and electronics engineering from the Middle East Technical University, Ankara, Turkey, in 2007 and 2010, respectively, and the Ph.D. degree in electronics and telecommunications engineering from Kocaeli University, Izmit, Turkey, in 2013.

He was a Postdoctoral Researcher with the Hyperspectral Computing Laboratory (HyperComp), University of Extremadura, Cáceres, Spain. He is currently an Assistant Professor with the Department of Electronics and Telecommunications Engineering, Kocaeli University. His research interests include digital image processing, remote sensing, and hyperspectral imaging.



**Marian-Daniel Iordache** received the M.Sc. degree in electrical engineering from the Politehnica University of Bucharest, Bucharest, Romania, in 2006, and the Ph.D. degree in electrical and computer engineering from the Instituto Superior Tecnico, Lisbon, Portugal, in 2011.

In 2006, he was with the Electrical Engineering Research Center, Bucharest, Romania, where he worked on several national and European projects dedicated to microelectromechanical systems and high-frequency circuits. From 2008 to 2011, he was a Marie Curie Fellow with the Hyperspectral Imaging Network project funded by the European Commission under the Sixth Framework Programme. Since 2010, he has been a member of the Hyperspectral Computing Laboratory Research Group, University of Extremadura, Cáceres, Spain. He is currently a Researcher with the Flemish Institute for Technological Research, Center for Remote Sensing and Earth Observation Processes (TAP), Mol, Belgium. His research interests include hyperspectral data processing and unmixing, with emphasis on the sparse characteristics of the solutions.

Dr. Iordache was awarded with the prize The Romanian Student of the Year in Europe 2011, offered by the League of Romanian Students Abroad, for his research activity and social implication.



**Antonio Plaza** (M'05–SM'07–F'15) received the M.S. and Ph.D. degrees in computer engineering from the University of Extremadura, Cáceres, Spain, in 1999 and 2002, respectively.

He was a Visiting Researcher at the Remote Sensing Signal and Image Processing Laboratory, University of Maryland, Baltimore County, Baltimore, MD, USA, the Applied Information Sciences Branch, Goddard Space Flight Center, Greenbelt, MD, USA, and the AVIRIS Data Facility, Jet Propulsion Laboratory, Pasadena, CA, USA. He is currently an Associate Professor with the Department of Technology of Computers and Communications, University of Extremadura, where he is the Head of the Hyperspectral Computing Laboratory. He was the Coordinator of the Hyperspectral Imaging Network, a European project designed to build an interdisciplinary research community focused on hyperspectral imaging activities. He has been a Proposal Reviewer with the European Commission, the European Space Agency, and the Spanish Government. He is the author or coauthor of around 350 publications on remotely sensed hyperspectral imaging, including more than 70 journal citation report papers, 20 book chapters, and over 200 conference proceeding papers. His research interests include remotely sensed hyperspectral imaging, pattern recognition, signal and image processing, and efficient implementation of large-scale scientific problems on parallel and distributed computer architectures.

Dr. Plaza has coedited a book on high-performance computing in remote sensing and guest edited seven special issues on remotely sensed hyperspectral imaging for different journals, including the IEEE TRANSACTIONS ON GEOSCIENCE AND REMOTE SENSING (for which he serves as Associate Editor on hyperspectral image analysis and signal processing since 2007), the IEEE JOURNAL OF SELECTED TOPICS IN APPLIED EARTH OBSERVATIONS AND REMOTE SENSING, the *International Journal of High-Performance Computing Applications*, and the *Journal of Real-Time Image Processing*. He has served as a Reviewer for more than 280 papers submitted to more than 50 different journals, including more than 140 papers reviewed for the IEEE TRANSACTIONS ON GEOSCIENCE AND REMOTE SENSING. He has served as a Chair for the IEEE Workshop on Hyperspectral Image and Signal Processing: Evolution in Remote Sensing in 2011. He has also been serving as a Chair for the SPIE Conference on Satellite Data Compression, Communications, and Processing since 2009, and for the SPIE Remote Sensing Europe Conference on High-Performance Computing in Remote Sensing since 2011. He is currently serving as an Editor of the IEEE TRANSACTIONS ON GEOSCIENCE AND REMOTE SENSING. He was the recipient of the recognition of Best Reviewers of the IEEE GEOSCIENCE AND REMOTE SENSING LETTERS in 2009, and the recognition of Best Reviewers of the IEEE TRANSACTIONS ON GEOSCIENCE AND REMOTE SENSING in 2010.